Zitierweise: *Angew. Chem. Int. Ed.* **2023**, *62*, e202218189
Internationale Ausgabe: doi.org/10.1002/anie.202218189
Deutsche Ausgabe: doi.org/10.1002/ange.202218189

Prebiotic Hydrothermal Reactions

Influence of Composition of Nickel-Iron Nanoparticles for Abiotic CO_2 Conversion to Early Prebiotic Organics

*Tuğçe Beyazay, Cristina Ochoa-Hernández, Youngdong Song, Kendra S. Belthle, William F. Martin, and Harun Tüysüz**

Abstract: Abiotic synthesis of formate and short hydrocarbons takes place in serpentinizing vents where some members of vent microbial communities live on abiotic formate as their main carbon source. To better understand the catalytic properties of Ni–Fe minerals that naturally exist in hydrothermal vents, we have investigated the ability of synthetic Ni–Fe based nanoparticular solids to catalyze the H_2-dependent reduction of CO_2, the first step required for the beginning of prebiotic chemistry. Mono and bimetallic Ni–Fe nanoparticles with varied Ni-to-Fe ratios transform CO_2 and H_2 into intermediates and products of the acetyl-coenzyme A pathway—formate, acetate, and pyruvate—in mM range under mild hydrothermal conditions. Furthermore, Ni–Fe catalysts converted CO_2 to similar products without molecular H_2 by using water as a hydrogen source. Both CO_2 chemisorption analysis and post-reaction characterization of materials indicate that Ni and Fe metals play complementary roles for CO_2 fixation.

Introduction

Because of their reactive chemical environment, hydrothermal vents are interesting in the context of life's origin.[1,2] They harbor microbial communities that might reflect growth conditions on the early Earth,[3,4] with chemosynthetic primary production powered by reactions of inorganic compounds provided by their habitat.[5] Off ridge systems like the Lost City Hydrothermal Field present highly reducing, alkaline and cooler conditions[6] relative to black smokers, which tend to be situated directly above volcanic activity at spreading zones, and are therefore the focus of theories that aim to narrow the gaps between geochemical and biological processes.[6–10] The chemistry of the Lost City type hydrothermal vents is marked by the geochemical process of serpentinization, in which reactions of water with olivine-rich (magnesium iron silicate) ultramafic rocks generate metal oxides, aqueous hydroxides and H_2 gas as a key byproduct.[8,9] H_2 synthesized during serpentinization can generate high concentrations of formate, which is the main carbon source for microbial growth in some serpentinizing systems.[10–14] H_2 generated during serpentinization can also reduce metal ions in the crust (like Fe^{2+} and Ni^{2+}) directly to their native metals or alloys. For example, Ni_3Fe alloy (awaruite) can be formed naturally at 50 bars of H_2 partial pressure at low temperature.[15] Although awaruite is the most commonly reported alloy,[16–18] also existence of various combinations of Fe–Ni alloys like taenite,[19] tetrataenite,[20] and their native metal forms in hydrothermal vent systems have been reported.[21,22]

The continuous production of molecular H_2 at concentrations between 1–15 mmol kg^{-1} is thought to play a critical role for early metabolic evolution[23,24] because the most ancient biochemical pathway of CO_2 fixation, the linear acetyl-coenzyme A (acetyl-CoA) pathway, utilizes H_2 as an electron donor.[25] The acetyl-CoA pathway is the only exergonic autotrophic CO_2 fixation pathway known.[26,27] The central and most highly conserved enzyme of the acetyl-CoA pathway is bifunctional carbon monoxide dehydrogenase/acetyl-CoA synthase (CODH/ACS), which is replete with transition metal (Ni, Fe) sulfide clusters at its active sites,[28,29] suggesting that these metals might have served as inorganic catalysts for the pathway prior to the origin of enzymes.

Reductants released from hydrothermal vents, such as H_2S[30] and H_2, can convert CO_2 to small organic molecules under hydrothermal conditions with the help of transition metal catalysts. It has been demonstrated that zero valent metals like Mn,[31] Fe, and Ni[32] can reduce CO_2 at relatively high temperatures (ranging 200–300 °C) when HCO_3^- is used as carbon source in water. Horita and Berndt reported in 1999 that Ni_3Fe (awaruite) is able to reduce CO_2 to CH_4 in H_2-rich aqueous solution at 300 °C under 500 bar, which suggested a source for the origin of abiotic CH_4 in vent effluent.[33] He et al. reported the synthesis of formate and acetate from aqueous CO_2 using

[*] T. Beyazay, Dr. C. Ochoa-Hernández, Dr. Y. Song, K. S. Belthle, Priv.-Doz. Dr. H. Tüysüz
Department of Heterogeneous Catalysis,
Max-Planck-Institut für Kohlenforschung
Kaiser-Wilhelm-Platz 1, 45470 Mülheim an der Ruhr (Germany)
E-mail: tueysuez@kofo.mpg.de
Prof. W. F. Martin
Institute of Molecular Evolution, University of Düsseldorf
40225 Düsseldorf (Germany)

native iron as the reductant.[34] Roldan et al. reported electrochemical CO_2 reduction in H_2O over Fe_3S_4 catalyst to formate, acetate, pyruvate, and methanol (compounds of the acetyl-CoA pathway) with micromolar yields at different pH values.[35] Moran and co-workers found CO_2 fixation using native transition metals Ni^0, Fe^0 and Co^0 as reductants, yielding formate, acetate and pyruvate with 1–40 bar of CO_2 at the temperature range of 30–100 °C.[36] Recently, Preiner et al. demonstrated that hydrothermal vent minerals, FeS, Fe_3O_4, and Ni_3Fe are able to reduce CO_2 to 200 mM formate, 100 μM acetate, and 10 μM pyruvate using H_2 as a reductant under mild hydrothermal conditions, at 25 bar and 100 °C, directly emulating the H_2-dependent acetyl-CoA reaction pathway used by microbes.[37] Hudson et al. reported pH-dependent CO_2 reduction to ≈1 μM formate using an Fe(Ni)S catalyst.[38] Later, He et al. reported the abiotic formation of long-chain hydrocarbons from $NaHCO_3$ by using Co and Fe catalysts.[39] This progress in the field of metal-dependent CO_2 reduction in the context of the origins has not been accompanied by systematic investigations of the effects of the composition of iron and nickel in their alloys. Furthermore, the role of H_2O as potential hydrogen and oxygen source in the absence of H_2 for CO_2 fixation has not been explored. Besides its importance for life, CO_2 is also a potential greenhouse gas,[40,41] the use of which as possible feedstock for the synthesis of value-added chemicals can lower the carbon footprint.[42,43] Understanding of abiotic CO_2 conversion to organics in hydrothermal vents can also provide insights towards the development of sustainable CO_2 reduction systems.

We recently investigated the formation of pyruvate from $CO_2 + H_2$ and the conversion of this C3 product to a larger molecule, citramalate, over Ni_3Fe catalyst in water at 25 °C.[44] Herein, we focus on the different compositions of Ni–Fe catalysts for CO_2 reduction in the presence or absence of molecular H_2. Thus, we examine the hard-templating synthesis of a range of iron and nickel based monometallic and bimetallic nanoparticles (Ni_3Fe, NiFe and $NiFe_3$) with similar morphology and textural parameters and their use as tools to establish catalyst composition-activity correlations for CO_2 fixation. Effects of reaction parameters on the product formation were systematically studied. In addition, the alteration of the catalyst post-reaction and the interaction of CO_2 with the metal catalyst were studied for better understanding of the reaction and its mechanism. We also explore whether water can serve as a reductant under simulated hydrothermal vent conditions to generate CO_2 fixation products. All of the catalysts produced significant amounts of formate, acetate and pyruvate at 100 °C and 25 bar in the presence of molecular H_2. Bimetallic Ni–Fe alloys showed superior activity and stability compared to their counterparts for CO_2 fixation. In addition, Ni and Fe nanoparticles were able to reduce CO_2 in H_2O without the addition of molecular H_2. The findings contribute to understanding of CO_2 fixation to metabolic intermediates in hydrothermal vents.

Results and Discussion

Since Ni–Fe metals exist in both hydrothermal vents and in the active center of carbon monoxide dehydrogenase (CODH) enzyme, a series of monometallic (Ni and Fe) and bimetallic (Ni_3Fe, NiFe and $NiFe_3$) oxide nanoparticles with similar morphologies and surface areas were prepared by using tea leaves as a natural hard template. The X-ray diffraction (XRD) pattern of pristine Ni and Ni-rich samples showed the reflections corresponding to NiO (Figure S1a). As Fe content is increased, reflections of Fe_2O_3 became more significant and only Fe precursor formed solely Fe_2O_3 phase, as expected. After the reduction post-treatment with Ar/H_2 gas (90/10, 100 mL min^{-1}) at temperature of 500 °C, metal oxides were reduced to their metallic forms without presence of any noticeable oxide reflections (Figure S2a). The two reflections around 44.5° and 52° in the pure Ni sample correspond to (111) and (200) planes of Ni metal, respectively. Fe atoms easily dissolved in Ni lattice due to their crystallographic similarity and atomic radius (0.163 and 0.126 nm for Ni and Fe, respectively).[45] The incorporation of Fe atom into Ni structure leads to the expansion of Ni lattice and shift of (111) reflection to lower 2θ (Figure S2a). Nitrogen-sorption measurements of the oxides and reduced samples are presented in Figure S1b and S2b, respectively. The presence of hysteresis loop indicates that Ni–Fe nanoparticles retain their interparticle porosity after the H_2-reduction. BET surface areas of oxides and reduced samples were found to be around 80 and 30 $m^2 g^{-1}$, respectively. The H_2-reduction at 500 °C led to a significant decrease in the specific surface areas. The complete reduction of oxides to the corresponding zero valent metals can result in sintering since most metals agglomerates easily under elevated temperature conditions. The increase in Fe content in the Ni–Fe alloys did not significantly change the surface area. The morphology and crystallinity of nanoparticles were further validated by high-resolution transmission electron microscopy (HR-TEM) (Figure S3). The TEM images show sintered nanoparticles with particle sizes of around 10–20 nm for all samples. HR-TEM revealed highly crystalline Ni_3Fe particles with a *d-spacing* of 0.205 nm, which corresponds to the lattice plane of Ni_3Fe (111). For NiFe and $NiFe_3$, *d-spacing* of 0.207 nm and 0.206 nm were found, which correspond to 111 planes of NiFe and $NiFe_3$, respectively (Figure S3d–f). Scanning electron microscopy with energy dispersive X-ray spectroscopy (SEM-EDX) analysis and elemental mapping of mixed alloy samples show homogeneous distribution of nickel and iron with the targeted compositions (Figure S4).

After the structural and physicochemical characterization, catalytic abilities of Ni–Fe nanoparticles for CO_2 reduction under mild hydrothermal vent conditions are further studied by using a custom-made batch reactor that is shown in Figure S5. Gaseous CO_2 is used as substrate since it is considered to be the initial carbon source in bacteria.[46,47] All the reactions mentioned in this study were performed in an autoclave made of Mo–Ni contain-

ing alloy. To observe any catalytic effect coming from the experimental setup, several control experiments were conducted in the absence of either the native metal catalyst or CO_2 gas. None of the control reactions showed any significant amount of product formation (Figure S6). Among targeted products, formate and acetate were detected with very low concentrations that were close to the detection limit of high performance liquid chromatography (HPLC). This small background was not taken into account since the catalytically obtained formate and acetate concentrations were much higher over the metal catalyst.

The catalytic activities of synthesized Ni–Fe particles were examined systematically. Standard solutions of reference compounds, including the possible CO_2 reduction products, were analyzed by HPLC and ^{1}H NMR (Figure S7 and S8), and their corresponding retention times are presented in Table S1. First, the impact of catalyst composition on the product distribution of CO_2 fixation was evaluated at the reaction temperature of 100 °C under 25 bar gas mixture of 3:2 CO_2:H_2 (P_{final} is 30 bar) for 24 h. Figure 1a displays the total product concentrations obtained with HPLC over different catalysts. All Ni–Fe alloys tested yield formate as main product in concentrations varying between 38.7–55.5 mM after 24 h. The existence of the targeted key products like formate, acetate and pyruvate was also confirmed by ^{1}H NMR (Figure S9). High concentrations of formate are expected in the aqueous phase since the formation of this product is favorable for reactions performed in H_2O ($\Delta G = -0.4$ kJ mol^{-1}).[48,49]

Although the highest formate amount was obtained over Ni_3Fe, the highest concentration of acetate (0.7 mM) and pyruvate (0.1 mM) were attained over pristine Ni^0 catalyst. The incorporation of Fe into Ni lattice structure giving rise to the Ni_3Fe alloy favors the formation of much higher formate; however, further increase in Fe content (NiFe and $NiFe_3$) caused the decrement of the total product concentration as seen in Figure 1a.

Evidently, Fe and Ni metals play different and complementary roles in the alloys for CO_2 reduction reaction. Yadav and Kharkara previously suggested that a charge transfer from more electropositive Fe to Ni strengths metal-carbon bonding by increasing electron density on Ni.[50] Another factor that plays a significant role in the performance of Ni–Fe catalysts in CO_2 reduction is the higher oxygen affinity of Fe compared to Ni.[45] It has been proposed that Ni atoms can activate the carbon while Fe sites facilitates H_2O reduction to H_2 by adsorbing O_2.[45] This goes in line with the biological system where the reversible conversion of H_2 to protons and electrons is catalyzed by [NiFe] hydrogenases. Crystallographic studies on [NiFe] hydrogenases indicated that both Ni and Fe centers involved dissociation of H_2 to protons and electrons.[51] Difference between Ni and Fe metals for CO_2 hydrogenation will be discussed in more details below. Besides the liquid product analyses, gaseous products of the reaction over solid catalysts after 24 h were further analyzed by gas chromatography (GC),

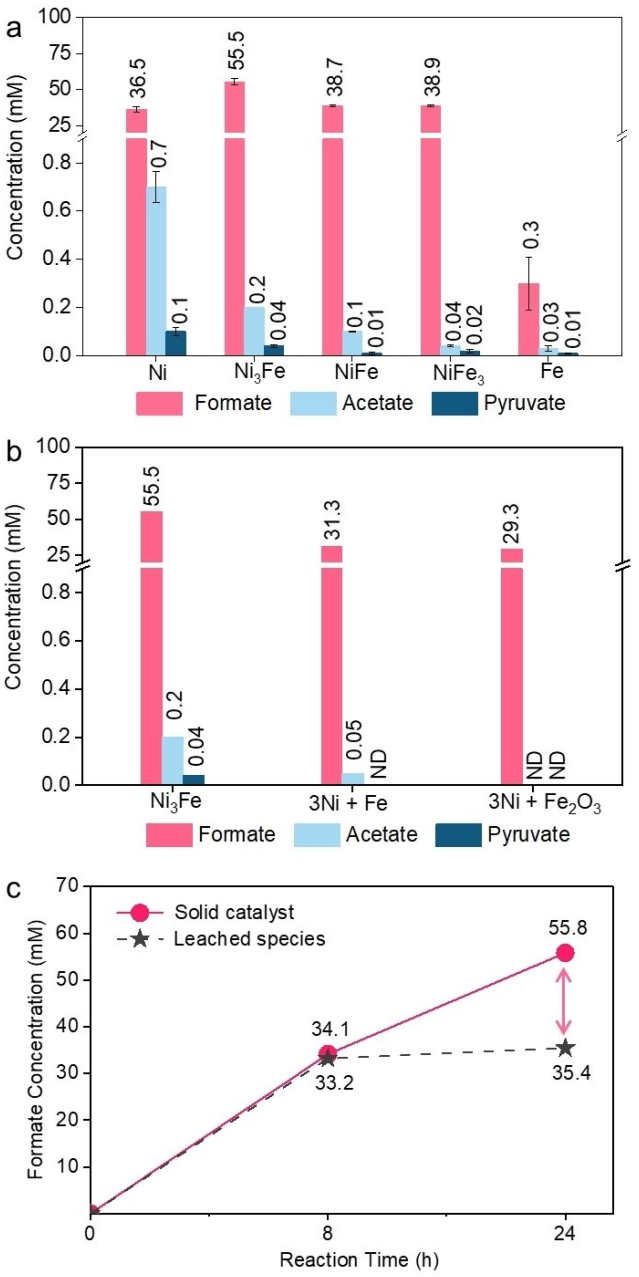

Figure 1. Product concentrations over Ni–Fe particles under 25 bar of $CO_2 + H_2$ gas mixture (CO_2:H_2 ratio is 3:2) at 100 °C for 24 h, based on HPLC analyses (a). Product concentration comparison of Ni_3Fe alloy and physical mixtures of Ni with Fe and Fe_2O_3 (b). Effect of Ni_3Fe solid catalyst and leached species on formate formation (c). Error bars are obtained from standard deviations of three independent reactions.

whereby CH_4 was detected as the main product over all Ni-containing catalysts (Figure S10). The highest CH_4 content (up to 0.25 mM) was obtained over native Ni metal catalyst (Figure S11) due to the known ability of Ni for CO_2 methanation.[52,53] The amount of the CH_4 formation decreased gradually with increasing Fe amount and pristine Fe catalyst did not yield any CH_4, which further revealed different catalytic behaviors of Ni and Fe for CO_2 fixation.

To explore whether product formation was promoted by alloying of Ni and Fe, three further experiments were designed under the same reaction conditions, namely at 100 °C and 25 bar for 24 h. The most active Ni_3Fe alloy, a physical mixture of native Ni and Fe in ratio of 3:1 and a physical mixture of native Ni with Fe_2O_3 (3:1) were used as catalysts (total metal loading was kept as 1 M). As seen in Figure 1b, while Ni_3Fe alloy yields formate (55.5 mM), acetate (0.2 mM) and pyruvate (0.04 mM) after 24 h, the physical mixture of Ni with Fe yielded only formate and acetate with lower concentrations (31.3 and 0.05 mM, respectively). No acetate or pyruvate formation was detected over the physical mixture of Ni and Fe_2O_3. Using Fe_2O_3 instead of metallic Fe resulted in a significant decrease in product concentrations. This supports that Fe^0 catalyst is more active than Fe_2O_3 for the CO_2 reduction under these experimental conditions. The catalytic difference between Ni_3Fe alloy and the physical mixture of Ni and Fe confirm that the interaction between Fe and Ni resulted in a structural variation of active sites, leading to a variation in the product selectivity.

A noticeable color change in the solution was observed after the catalytic reaction over the Ni_3Fe catalyst (Figure S12). In order to investigate the possible leaching of metal species and their potential catalytic contribution, the liquid reaction solution was analyzed by inductively coupled plasma—optical emission spectrometry (ICP-OES) after reaction and subsequently filtration of the solid catalyst. The solution after the reaction presented 27 $\mu g\,mL^{-1}$ Ni ions and 98 $\mu g\,mL^{-1}$ Fe. Although the Ni_3Fe catalyst has higher content of Ni, the level of Fe species in the reaction solution was almost four-fold higher. In addition, reaction solution color was turned to orange. This can be attributed to their standard oxidation potentials. While the standard oxidation potential of Fe/Fe^{2+} is +0.44 V, this value is +0.23 V for Ni/Ni^{2+}.[54,55] Therefore, the oxidation of metallic Fe is much easier in H_2O compared to metallic Ni. To investigate the potential catalytic role of these leached species, after 8 h of reaction time, the solid catalyst was removed via hot-filtration method and the reaction was continued for another 16 h without any solid catalyst. As seen in Figure 1c, the contribution of leached species towards further formation of formate is negligible compared to the solid catalyst, which indicates that native metal forms of Ni–Fe alloys are the active sites for CO_2 fixation instead of the leached Ni and Fe ions. The implemented reaction temperature and time scales bear upon the dynamic reaction in terms of product concentrations and reaction intermediates since the catalyst might undergo a structural change during the catalytic reaction. A set of experiments was carried out over native Fe and Ni catalysts with different reaction times of 8 h, 24 h, and 168 h. The outcome is illustrated in Figure 2. HPLC results showed that metallic Ni promotes the formation of formate (5.8 mM), acetate, and pyruvate after 8 h, while Fe^0 resulted in small amount of formate (0.2 mM) and did not yield any acetate or pyruvate. After 24 h of reaction time, formation of acetate and pyruvate were detected over metallic Fe nanoparticles

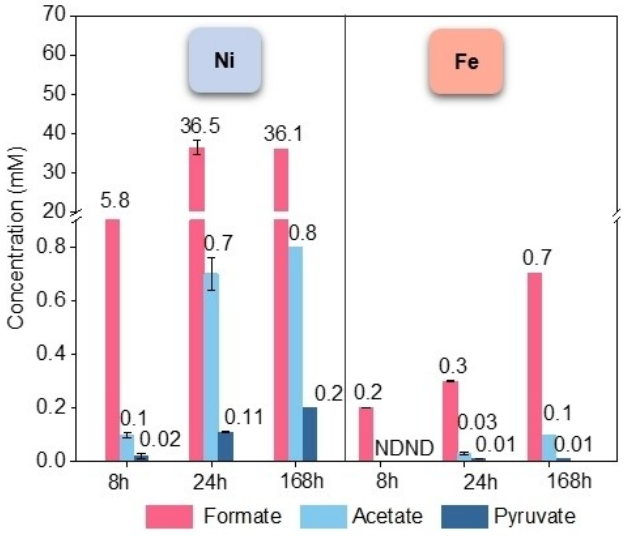

Figure 2. Time study for 8 h, 24 h, and 168 h over Ni and Fe metals (25 bar CO_2+H_2 mixture (3:2 ratio) at 100 °C). Error bars represent standard deviations of three independent reactions.

and product concentrations were increased over Ni^0 catalyst. However, further increase of reaction time to 168 h did not improve the product concentrations over Ni^0 catalysts.

To reveal the effect of time on bimetallic catalyst, Ni_3Fe, NiFe, and $NiFe_3$ were also exposed to long-term reaction time of 168 h (Figure S13). With increasing the reaction time, one would expect the enhancement of the product concentration of CO_2 fixation because of the large amount of CO_2 within the reactor vessel. However, this is not the case for the system with Ni_3Fe catalyst, which was the most active catalyst after 24 h of the reaction time. The reason might be attributed to the decomposition of synthesized products or deactivation of the catalyst, which will be further elaborated in detail in the below section of post-reaction characterization. At high temperature conditions, formic acid can be further decomposed to $CO+H_2O$ and CO_2+H_2 via decarbonylation and decarboxylation reactions, respectively.[56] Previous studies on formic acid decomposition in gas and aqueous phases showed that decarboxylation of formic acid to CO_2+H_2 is more favorable in water-containing reactions while the dehydration of formate to CO is more favorable in the gas-phase reactions.[57] In order to determine if formate decomposes in H_2O over Ni_3Fe catalyst, an additional experiment was performed at 100 °C under Ar atmosphere (25 bar) by using formic acid as a starting substrate. After 24 h of reaction time, 87 % of formic acid was converted, and dissolved CO_2 could be detected in reaction solution via HPLC analysis (Figure S14). Therefore, decarboxylation of formate over Ni_3Fe catalyst at 100 °C—along with the potential catalyst alteration—can be the reason of no further enhancement of product concentrations after 168 h.

The role of water and molecular H_2 for the CO_2 fixation over nanostructured catalysts was further investigated. During the serpentinization process, H_2 is formed from water reduction via the chemical oxidation of metal sites of natural minerals.[9] During the oxidation of metals in water, the hydronium ion is oxidized by the released electrons and forms hydrogen radicals. As discussed above, slight oxidation and leaching of Ni and Fe metals into the reaction solution was confirmed by ICP-OES. Therefore, the ability of selected catalysts (Ni, Ni_3Fe and Fe) to reduce CO_2 in H_2O without using molecular H_2 is further studied under mild hydrothermal vent conditions, 25 bar of CO_2 at 100 °C (P_{final} is 30 bar). As shown in Figure 3a, after the reaction time of 24 h, formate, acetate, and pyruvate could be obtained over Ni^0 and Ni_3Fe catalysts, while Fe^0 catalyst formed only formate. The synergistic effect between Ni and Fe is also observed in the reactions without starting molecular H_2, where the formate amount was more than doubled over Ni_3Fe catalyst compared to its monometallic counterparts. This activity is well-matched with the bimetallic active sites of natural enzymes, which catalyze challenging multi-electron transfer reactions, such as CO_2 reduction and N_2 activation.[58,59] CO_2 activation on [NiFe] carbon monoxide dehydrogenase is well established, where binding of CO_2 on Ni–Fe centers results in direct electron transfer from metal center (Ni) to the antibonding unoccupied orbital of CO_2 and increase in negative partial charge at the oxygen atom.[60] Oxygen is then stabilized by binding to electron-deficient Fe centers.[61] Although the products obtained are the same in molecular H_2-added reactions, concentrations of products were much lower in the absence of molecular H_2, which supports that the reaction is H_2-dependent. On the other hand, it was found that, the required H_2 for CO_2 reduction can be provided from H_2O splitting in the absence of molecular H_2, as naturally occurs in serpentinization process. The ability of the solid

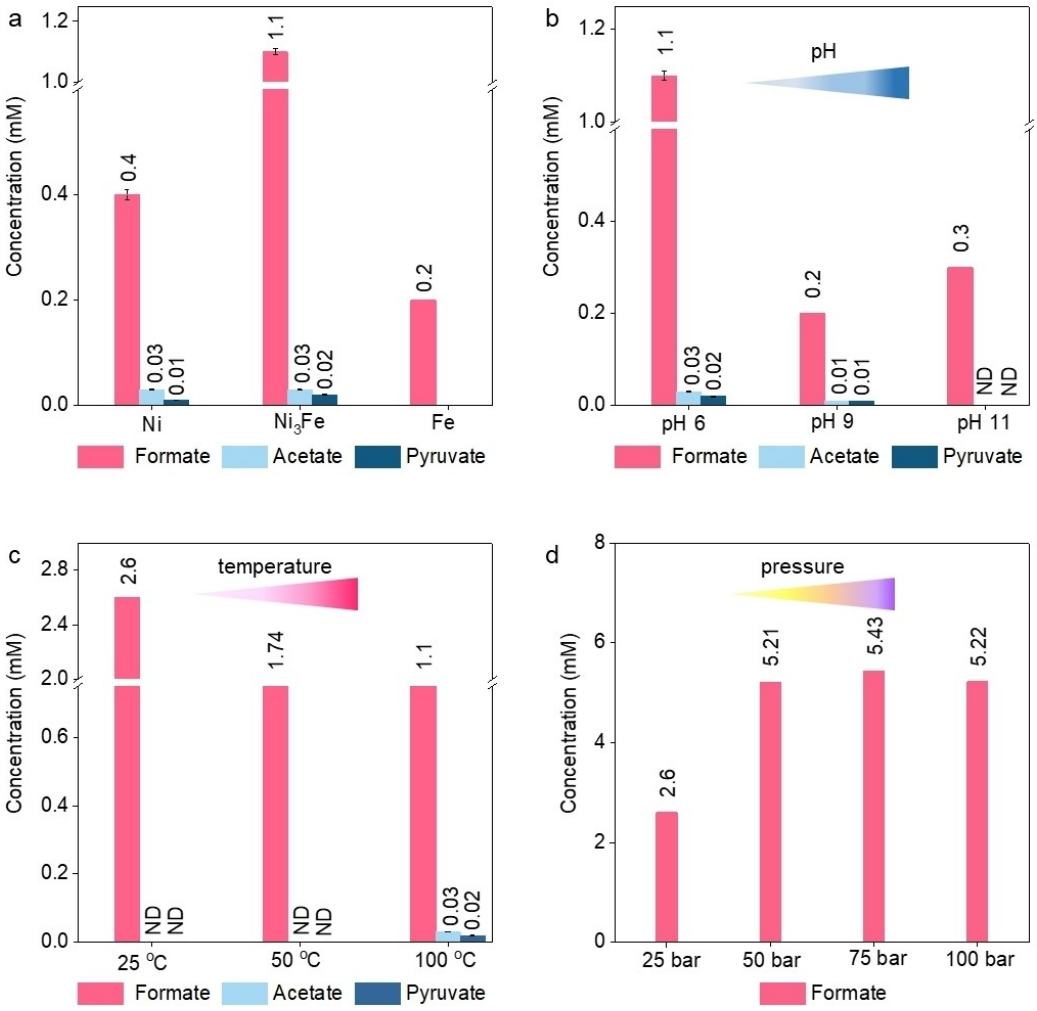

Figure 3. Concentrations of formate, acetate, and pyruvate obtained over Ni, Ni_3Fe, and Fe catalysts during the CO_2 reduction in H_2O without the addition of molecular H_2 under 25 bar of CO_2 at 100 °C (a). Comparison of product concentrations at: different pHs under 25 bar CO_2 and 100 °C (b), different temperatures under 25 bar of CO_2 (c) and different initial reaction pressures at 25 °C (d) over the selected Ni_3Fe catalyst for 24 h of reaction time. * ND: Not detected. Error bars are obtained from standard deviations of three independent reactions.

Ni_3Fe catalyst to split H_2O might have some similarities to reactions of [NiFe] hydrogenases.[51,62]

Temperature, reaction pressure, and pH were varied to explore their impact on product formation in the absence of molecular H_2. As seen in Figure 3b, pH of the reaction significantly alters the product concentrations, whereas lower concentrations are obtained over Ni_3Fe catalyst at higher pH values at 100 °C. Neither acetate nor pyruvate were obtained at pH 11. Although H_2-dependent CO_2 reduction is favorable under alkaline conditions, due to the redox potential drop of H_2 to $2H^+$ at higher pH,[63] Ni_3Fe-catalyzed formate formation was decreased under alkaline conditions. The possible reason for this trend is that the carbonic acid equilibrium in water is highly dependent on the pH of the solution. Dissolved CO_2 in H_2O can exist as carbonic acid, bicarbonate, and carbonate according to the carbonic acid equilibrium. Increasing pH shifts the carbonic acid equilibrium towards bicarbonate and carbonate. Dissolved CO_2 exists as CO_3^{2-} ion in solution with pH 11 and its conversion is more challenging due to its resonance structure.[64]

The impact of reaction temperature was further studied over the selected Ni_3Fe catalyst, whereby it was found that the decreasing reaction temperature from 100 °C to 50 and 25 °C under 25 bar of initial CO_2, significantly increased the formate concentration after 24 h of reaction time (Figure 3c). However, no acetate or pyruvate formation could be detected at lower temperatures. Low reaction temperature can be adverse for the enhancement of reaction rate due to the kinetic barriers of further conversion of acetate and pyruvate. Another reason for higher formate amount at lower temperatures might be the prevention of formate decomposition, which occurs at higher temperatures as aforementioned. After observing that formate could be obtained even at 25 °C and 25 bar of CO_2, the effect of CO_2 pressure was further investigated over Ni_3Fe catalyst at 25 °C. As above-mentioned, formate formation from CO_2 is exergonic in aqueous media, but the limited solubility of CO_2 in water under ambient conditions (Henry's constant, $K_H = 0.035\ M\,atm^{-1}$ at 25 °C) makes its conversion more challenging.[64] Likely, the solubility of CO_2 can be improved by increasing the initial partial pressure of the gas since the dissolved gas amount in aqueous solutions is proportional to the applied pressure according to Henry's law.[65] As seen in Figure 3d, increase of initial CO_2 pressure from 25 bar to 50 bar almost doubled the formate amount (from 2.6 mM to 5.21 mM). This result was expected since the amount of CO_2 was increased in a closed system, which caused the reaction equilibrium shift to products according to Le Chatelier's principle. However, further increase of CO_2 pressure to 75 bar and 100 bar did not change significantly the formate concentrations. Although dissolved gas amount increased in the reaction solution at higher pressure, it might reach to a saturation point with 50 bar of CO_2. Furthermore, H_2 is the limited reagent in these reactions due to the excess amount of CO_2. In addition, the excess amount of dissolved CO_2 might alter the surface of the catalyst, which will be further discussed in below. Therefore, H_2 production from H_2O might be prevented by deactivation of the active catalyst surface with high amount of dissolved CO_2. All in all, results from molecular H_2-free reactions prove the direct contribution of metal catalyst on CO_2 fixation in H_2O. Solid Ni–Fe particles can selectively reduce CO_2 to acetyl-CoA pathway intermediates in the presence or even in the absence of molecular H_2 in H_2O. Our finding clearly shows that some reactions of the naturally occurring serpentinization process can be simulated in laboratory under mild hydrothermal vent conditions. The catalytic survey indicated a clear composition-activity dependence of CO_2 fixation.

CO_2 temperature-programmed desorption (TPD) analysis can provide some insights about the interactions of CO_2 with the surface of solid catalysts, as well as temperature induced desorption profile of the CO_2 molecule. As seen in Figure 4, TPD profiles of Ni and Ni_3Fe show a large amount of desorbed CO_2 at temperature values of around 200 °C, which indicates the existence of moderate interactions.[66] CO_2 binding strengths on the Ni and Ni_3Fe look very similar, whereby a small shift to higher temperatures in the desorption signal of Ni_3Fe was observed, which hints an increase of binding strength of CO_2. No noticeable CO_2 desorption signal was observed above 200 °C for Ni and Ni_3Fe samples. Further addition of Fe modifies the interaction of the alloys and their TPD profiles, where an additional CO_2 desorption peak could be observed around 600 °C for NiFe and $NiFe_3$ samples, similar to pristine metallic Fe. Moreover, the amount of desorbed CO_2 at lower temperature decreased strongly for metallic Fe catalyst. Two distinct desorption peaks were observed at the temperature range of 500–700 °C, which indicates CO_2 species strongly bonded to the surface of Fe.[67] This kind of strong adsorption on the iron sites does not favor high catalytic conversion rates of CO_2 reduction, as seen from the catalytic survey of CO_2

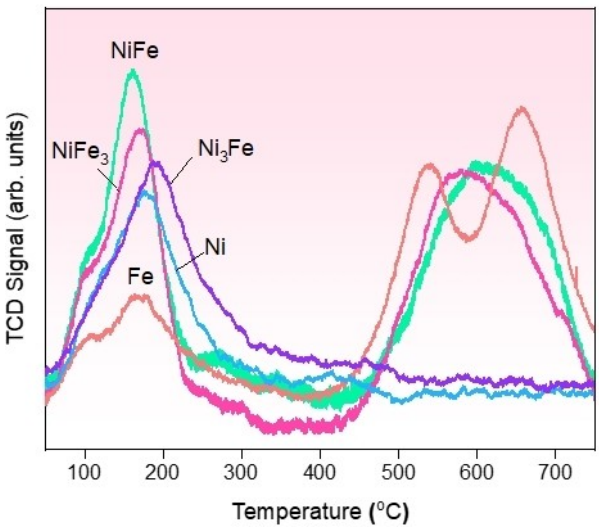

Figure 4. CO_2-TPD profiles of Ni^0, Ni_3Fe, NiFe, $NiFe_3$ and Fe^0 in the temperature range of 50–750 °C.

fixation over pristine Fe catalyst (Figure 1a). This could also cause strong alteration and deactivation of catalyst. On the other hand, combination of Fe with the Ni suppresses the presence of strong interactions at high temperatures for Ni_3Fe sample that shows the highest catalytic activity for the CO_2 conversion. To validate that the desorbed CO_2 peaks are solely originated from the introduced CO_2 during the measurements, a blank experiment was performed with $NiFe_3$ sample since it shows both weak and strong desorption peaks. For the blank test, the sample was subjected to the same protocol of analysis, but substituting the CO_2 gas flow by He. After heating the sample up to 750 °C, no noticeable desorbed species could be detected in the blank TPD test (Figure S15).

To investigate the metal catalysts alteration after the reaction, all the materials were further characterized by XRD and FTIR, and results are presented in Figure S16. XRD patterns of post-reaction catalysts prove the formation of crystalline $FeCO_3$ for all Fe-containing catalysts whereby no $NiCO_3$ formation was observed. The intensity of $FeCO_3$ (siderite) reflection rises with increasing Fe ratio within the catalyst. While there was not any change in monometallic Ni, Fe catalyst was almost completely converted to $FeCO_3$ after 24 h. The existence of $FeCO_3$ was further confirmed by FTIR analysis for all bimetallic Ni–Fe catalysts where the sharp peak around 880 cm^{-1} and broad band around 1450 cm^{-1} can be assigned to the CO_3^{2-} bending and asymmetric stretching of CO_3^{2-}, respectively (Figure S16b).[68] The highest CO_3^{2-} band intensity was observed for pristine Fe sample, which even changed its color to green/gray after the reaction (Figure S17). Previously reported DFT calculations on the comparison of CO_2 adsorption on Ni and Fe metals suggested stronger CO_2 chemisorption on Fe surface than Ni surface.[69] Our CO_2-TPD results of Ni and Fe metals, which suggested strong binding of CO_2 over Fe catalyst, are also consistent with the post-reaction characterization results. The strong binding of CO_2 on Fe catalyst deactivates its surface after 24 h and, therefore, the

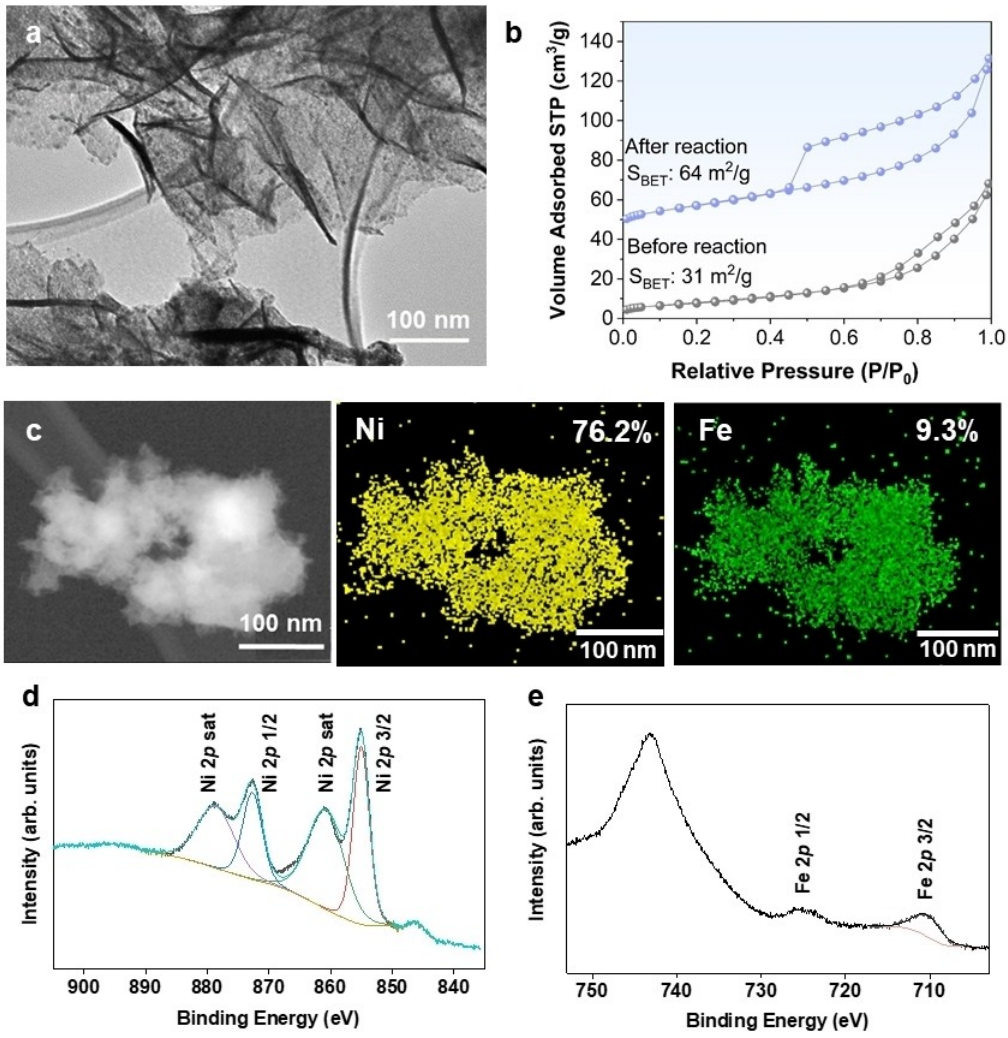

Figure 5. TEM image (a), N_2-sorption isotherm (offset: 50 $cm^3 g^{-1}$) (b), STEM image and EDX elemental mapping (c), and XPS spectra of Ni 2*p* (d) and Fe 2*p* (e) of Ni_3Fe catalyst after the reaction under 25 bar $CO_2 + H_2$ (3 : 2 ratio) at 100 °C for 24 h.

obtained product concentrations were much lower over monometallic Fe. In addition, on the basis of these experimental results, it can be proposed that the conversion of Fe to $FeCO_3$ and dissociation of water provide extra H_2 to the system following below Equations:[70]

$$CO_{2\,(g)} \rightleftharpoons CO_{2\,(aq)} \quad (1)$$

$$CO_{2\,(aq)} + H_2O\,(l) \rightleftharpoons HCO_3^-(aq) + H^+(aq) \quad (2)$$

$$Fe_{\,(s)} + 2H^+(aq) \rightleftharpoons Fe^{2+}(aq) + H_2(g) \quad (3)$$

$$Fe_{(s)} + CO_{2(g)} + H_2O_{(l)} \rightarrow FeCO_{3(s)} + H_{2(g)} \quad (4)$$

This further illustrates the ability of water for providing protons and forming hydrogen that can react with CO_2 to form carboxylic acids in the absence of starting molecular hydrogen in a closed reactor system. Furthermore, the existence of siderite ($FeCO_3$) after the reaction matches well with the existence of siderite in sediments close to hydrothermal vents.[71] Since Ni_3Fe shows the highest concentrations of targeted products, it was further characterized in detail after the catalytic reaction under 25 bar of CO_2+H_2 at 100 °C for 24 h. As seen in TEM image in Figure 5a, the morphology of the catalyst has been altered dramatically after 24 h of reaction time under pressurized CO_2. The initial nanoparticles morphology (Figure S3a) was transformed into small nanoparticle supported nanosheet structure. The alteration of the morphology also affected the BET surface area and hysteresis loop of Ni_3Fe after the CO_2 reduction reaction (Figure 5b). The BET surface area of Ni_3Fe catalyst increased by two-fold, from 31 to 64 m^2g^{-1}. In addition, STEM image and elemental mapping of Ni_3Fe showed the significant change of the morphology and the Ni to Fe ratio after the catalytic reaction (Figure 5c). The leaching of iron matches well with previously mentioned ICP-OES result of the reaction solution (Figure S12). The surface alteration of the Ni_3Fe catalyst after reaction could also be confirmed by X-ray photoelectron spectroscopy (XPS) analysis, as shown in Figure 5d. Ni 2p spectrum does not show any remaining metallic Ni on the surface after the reaction time and Fe 2p spectra shows mainly Fe^{3+} species (Figure 5d and e). Although the bulk analysis of Ni_3Fe did not show any oxidation product of Ni, XPS result indicates that the surface of the catalyst is oxidized after 24 h due to the aqueous reaction conditions. All results from post-reaction characterization of Ni–Fe catalysts indicate that Ni did not show significant change in terms of the bulk structure while Fe mostly converted to $FeCO_3$. Therefore, it can be proposed that Ni functions as main catalytic active sites for CO_2 hydrogenation to form key metabolic intermediates.

Conclusion

The reduction of CO_2 to prebiotically crucial organic compounds such as formate, acetate, pyruvate, and methane, in mM ranges, over Ni–Fe nanoparticles proceeds readily under simulated hydrothermal vent conditions. Our findings showed that Ni–Fe alloys, which exist in both active centers of hydrogenase enzymes and in hydrothermal vent minerals, can convert inorganic CO_2, H_2, and H_2O to biologically important small organic compounds. Bimetallic Ni_3Fe showed the superior performance compared to its counterparts Ni and Fe metals. This trend is similar to active sites of CODH enzyme. Different compositions of Ni–Fe alloys were also examined since they exist in hydrothermal vents with diverse compositions. The highest yield of formate, acetate, and pyruvate was obtained with the 3:1 ratio of Ni to Fe after 24 h reaction. Targeted products were obtained with or even without the addition of molecular H_2. In the absence of molecular H_2, H_2O acted as an electron donor, providing hydrogen that could further react with CO_2 over the nanostructured metal catalysts. Post-reaction characterization indicated that catalysts undergo surface and structural alteration, and iron carbonate formation could be detected for all iron containing samples. Under simulated hydrothermal vent conditions, Ni was found to act as the main catalytic site for CO_2 fixation and had much better stability towards oxidation and carbonate formation compared to native Fe nanoparticles. Hydrothermal formate is used as a growth substrate for some microbes that inhabit vent effluent. The laboratory reactions we report here might shed light on the source of that formate in natural systems.

Acknowledgements

This work is supported by Deutsche Forschungsgemeinschaft (MA-1426/21-1/TU 315/8-1) and the Volkswagen Foundation (96_742). We thank Prof. Joseph Moran for the fruitful discussion. Authors would like to thank Heike Hinrichs for HPLC measurements, and Dr. Christophe Fares and Jasmin Blenk for NMR characterizations. Authors thank Dr. Claudia Weidenthaler and Sebastian Leiting for XPS analysis. We also would like to acknowledge Eko Budiyanto, Adrian Schlüter, and Norbert Pfänder for microscopy images and Florian Baum for ICP-OES measurements. HT thanks FUNCAT Centre and Max Planck Society for the basic funding. Open Access funding enabled and organized by Projekt DEAL.

Conflict of Interest

The authors declare no conflict of interest.

Data Availability Statement

The data that support the findings of this study are available from the corresponding author upon reasonable request.

Keywords: Awaruite · CO_2 Reduction · Hydrothermal Vents · Serpentinization

[1] J. B. Corliss, J. Dymond, L. I. Gordon, J. M. Edmond, R. P. von Herzen, R. D. Ballard, K. Green, D. Williams, A. Bainbridge, K. Crane, T. H. van Andel, *Science* **1979**, *203*, 1073–1083.

[2] F. N. Spiess, K. C. Macdonald, T. Atwater, R. Ballard, A. Carranza, D. Cordoba, C. Cox, V. M. D. Garcia, J. Francheteau, J. Guerrero, J. Hawkins, R. Haymon, R. Hessler, T. Juteau, M. Kastner, R. Larson, B. Luyendyk, J. D. Macdougall, S. Miller, W. Normark, J. Orcutt, C. Rangin, *Science* **1980**, *207*, 1421–1433.

[3] K. S. Belthle, H. Tüysüz, *ChemCatChem* **2023**, *15*, e202201462.

[4] G. J. Dick, *Nat. Rev. Microbiol.* **2019**, *17*, 271–283.

[5] Z. Minic, P. D. Thongbam, *Mar. Drugs* **2011**, *9*, 719–738.

[6] W. Martin, J. Baross, D. Kelley, M. J. Russell, *Nat. Rev. Microbiol.* **2008**, *6*, 805–814.

[7] M. J. Russell, A. J. Hall, *Evolution of Early Earth's Atmosphere, Hydrosphere, And Biosphere: Constraints from Ore Deposits*, Geological Society of America, Boulder, **2006**, pp. 1–32.

[8] M. Preiner, J. Xavier, F. Sousa, V. Zimorski, A. Neubeck, S. Lang, H. Greenwell, K. Kleinermanns, H. Tüysüz, T. McCollom, N. Holm, W. Martin, *Life* **2018**, *8*, 41.

[9] M. J. Russell, A. J. Hall, W. Martin, *Geobiology* **2010**, *8*, 355–371.

[10] S. Q. Lang, G. L. Früh-Green, S. M. Bernasconi, W. J. Brazelton, M. O. Schrenk, J. M. McGonigle, *Sci. Rep.* **2018**, *8*, 755.

[11] S. Suzuki, K. H. Nealson, S. Ishii, *Front. Microbiol.* **2018**, *9*, 3141.

[12] D. R. Colman, E. A. Kraus, P. H. Thieringer, K. Rempfert, A. S. Templeton, J. R. Spear, E. S. Boyd, *Proc. Natl. Acad. Sci. USA* **2022**, *119*, e2206845119.

[13] W. J. Brazelton, J. M. McGonigle, S. Motamedi, H. L. Pendleton, K. I. Twing, B. C. Miller, W. J. Lowe, A. M. Hoffman, C. A. Prator, G. L. Chadwick, R. E. Anderson, E. Thomas, D. A. Butterfield, K. A. Aquino, G. L. Früh-Green, M. O. Schrenk, S. Q. Lang, *Appl. Environ. Microbiol.* **2022**, *88*, e0092922.

[14] M. K. Nobu, R. Nakai, S. Tamazawa, H. Mori, A. Toyoda, A. Ijiri, S. Suzuki, K. Kurokawa, Y. Kamagata, H. Tamaki, *ISME J.* **2023**, *17*, 95–104.

[15] N. H. Sleep, A. Meibom, T. Fridriksson, R. G. Coleman, D. K. Bird, *Proc. Natl. Acad. Sci. USA* **2004**, *101*, 12818–12823.

[16] R. Britten, *Econ. Geol.* **2017**, *112*, 517–550.

[17] J. C. Alt, W. C. Shanks, *Geochim. Cosmochim. Acta* **2003**, *67*, 641–653.

[18] F. Klein, W. Bach, *J. Petrol.* **2009**, *50*, 37–59.

[19] B. R. Frost, *J. Petrol.* **1985**, *26*, 31–63.

[20] A. Smirnov, D. Hausner, R. Laffers, D. R. Strongin, M. A. A. Schoonen, *Geochem. Trans.* **2008**, *9*, 5.

[21] V. Dekov, *J. Geophys. Res. Solid Earth* **2006**, *111*, B05103.

[22] J. F. Pernet-Fisher, J. M. D. Day, G. H. Howarth, V. V. Ryabov, L. A. Taylor, *Earth Planet. Sci. Lett.* **2017**, *460*, 201–212.

[23] D. S. Kelley, J. A. Karson, G. L. Früh-Green, D. R. Yoerger, T. M. Shank, D. A. Butterfield, J. M. Hayes, M. O. Schrenk, E. J. Olson, G. Proskurowski, M. Jakuba, A. Bradley, B. Larson, K. Ludwig, D. Glickson, K. Buckman, A. S. Bradley, W. J. Brazelton, K. Roe, M. J. Elend, A. Delacour, S. M. Bernasconi, M. D. Lilley, J. A. Baross, R. E. Summons, S. P. Sylva, *Science* **2005**, *307*, 1428–1434.

[24] M. O. Schrenk, W. J. Brazelton, S. Q. Lang, *Rev. Mineral. Geochem.* **2013**, *75*, 575–606.

[25] M. J. Russell, W. Martin, *Trends Biochem. Sci.* **2004**, *29*, 358–363.

[26] I. A. Berg, D. Kockelkorn, W. H. Ramos-Vera, R. F. Say, J. Zarzycki, M. Hügler, B. E. Alber, G. Fuchs, *Nat. Rev. Microbiol.* **2010**, *8*, 447–460.

[27] K. B. Muchowska, S. J. Varma, J. Moran, *Chem. Rev.* **2020**, *120*, 7708–7744.

[28] S. W. Ragsdale, M. Kumar, *Chem. Rev.* **1996**, *96*, 2515–2540.

[29] H. Dobbek, V. Svetlitchnyi, L. Gremer, R. Huber, O. Meyer, *Science* **2001**, *293*, 1281–1285.

[30] R. He, B. Hu, H. Zhong, F. Jin, J. Fan, Y. H. Hu, Z. Jing, *Chem. Commun.* **2019**, *55*, 1056–1059.

[31] L. Lyu, X. Zeng, J. Yun, F. Wei, F. Jin, *Environ. Sci. Technol.* **2014**, *48*, 6003–6009.

[32] F. Jin, Y. Gao, Y. Jin, Y. Zhang, J. Cao, Z. Wei, R. L. Smith, *Energy Environ. Sci.* **2011**, *4*, 881–884.

[33] J. Horita, M. E. Berndt, *Science* **1999**, *285*, 1055–1057.

[34] C. He, G. Tian, Z. Liu, S. Feng, *Org. Lett.* **2010**, *12*, 649–651.

[35] A. Roldan, N. Hollingsworth, A. Roffey, H.-U. Islam, J. B. M. Goodall, C. R. A. Catlow, J. A. Darr, W. Bras, G. Sankar, K. B. Holt, G. Hogarth, N. H. de Leeuw, *Chem. Commun.* **2015**, *51*, 7501–7504.

[36] S. J. Varma, K. B. Muchowska, P. Chatelain, J. Moran, *Nat. Ecol. Evol.* **2018**, *2*, 1019–1024.

[37] M. Preiner, K. Igarashi, K. B. Muchowska, M. Yu, S. J. Varma, K. Kleinermanns, M. K. Nobu, Y. Kamagata, H. Tüysüz, J. Moran, W. F. Martin, *Nat. Ecol. Evol.* **2020**, *4*, 534–542.

[38] R. Hudson, R. de Graaf, M. Strandoo Rodin, A. Ohno, N. Lane, S. E. McGlynn, Y. M. A. Yamada, R. Nakamura, L. M. Barge, D. Braun, V. Sojo, *Proc. Natl. Acad. Sci. USA* **2020**, *117*, 22873–22879.

[39] D. He, X. Wang, Y. Yang, R. He, H. Zhong, Y. Wang, B. Han, F. Jin, *Proc. Natl. Acad. Sci. USA* **2021**, *118*, e2115059118.

[40] K. S. Lackner, *Science* **2003**, *300*, 1677–1678.

[41] C. Hepburn, E. Adlen, J. Beddington, E. A. Carter, S. Fuss, N. Mac Dowell, J. C. Minx, P. Smith, C. K. Williams, *Nature* **2019**, *575*, 87–97.

[42] G. Prieto, *ChemSusChem* **2017**, *10*, 1056–1070.

[43] L. Wang, E. Guan, Y. Wang, L. Wang, Z. Gong, Y. Cui, X. Meng, B. C. Gates, F.-S. Xiao, *Nat. Commun.* **2020**, *11*, 1033.

[44] T. Beyazay, K. S. Belthle, C. Farès, M. Preiner, J. Moran, W. F. Martin, H. Tüysüz, *Nat. Commun.* **2023**, *14*, 570.

[45] D. Shi, R. Wojcieszak, S. Paul, E. Marceau, *Catalysts* **2019**, *9*, 451.

[46] M. Roger, F. Brown, W. Gabrielli, F. Sargent, *Curr. Biol.* **2018**, *28*, 140–145.

[47] L. B. Maia, L. Fonseca, I. Moura, J. J. G. Moura, *J. Am. Chem. Soc.* **2016**, *138*, 8834–8846.

[48] S. Moret, P. J. Dyson, G. Laurenczy, *Nat. Commun.* **2014**, *5*, 4017.

[49] P. G. Jessop, T. Ikariya, R. Noyori, *Nature* **1994**, *368*, 231–233.

[50] G. D. Yadav, M. R. Kharkara, *Appl. Catal. A* **1995**, *126*, 115–123.

[51] R. Das, F. Neese, M. van Gastel, *Phys. Chem. Chem. Phys.* **2016**, *18*, 24681–24692.

[52] L. Shen, J. Xu, M. Zhu, Y. F. Han, *ACS Catal.* **2020**, *10*, 14581–14591.

[53] C. Lv, L. Xu, M. Chen, Y. Cui, X. Wen, Y. Li, C. Wu, B. Yang, Z. Miao, X. Hu, Q. Shou, *Front. Chem.* **2020**, *8*, 269.

[54] S. G. Bratsch, *J. Phys. Chem. Ref. Data* **1989**, *18*, 1–21.

[55] A. Kraft, Y. Pernia, A. Kalio, A. Gautrein, L. Ni, J. Bartsch, S. Glunz, H. Reinecke, *J. Appl. Electrochem.* **2015**, *45*, 95–104.

[56] Y. Yasaka, K. Yoshida, C. Wakai, N. Matubayasi, M. Nakahara, *J. Phys. Chem. A* **2006**, *110*, 11082–11090.

[57] N. Akiya, P. E. Savage, *AIChE J.* **1998**, *44*, 405–415.

[58] S. W. Ragsdale, *Chem. Rev.* **2006**, *106*, 3317–3337.

[59] B. M. Hoffman, D. Lukoyanov, Z.-Y. Yang, D. R. Dean, L. C. Seefeldt, *Chem. Rev.* **2014**, *114*, 4041–4062.
[60] J.-H. Jeoung, H. Dobbek, *Science* **2007**, *318*, 1461–1464.
[61] Z. N. Zahran, E. A. Mohamed, Y. Naruta, *Sci. Rep.* **2016**, *6*, 24533.
[62] W. Lubitz, H. Ogata, O. Rüdiger, E. Reijerse, *Chem. Rev.* **2014**, *114*, 4081–4148.
[63] R. Vasiliadou, N. Dimov, N. Szita, S. F. Jordan, N. Lane, *Interface Focus* **2019**, *9*, 20190073.
[64] M. König, J. Vaes, E. Klemm, D. Pant, *iScience* **2019**, *19*, 135–160.
[65] R. Farajzadeh, P. L. J. Zitha, H. Bruining, *Ind. Eng. Chem. Res.* **2009**, *48*, 6423–6431.
[66] S. S. Ndlela, H. B. Friedrich, M. N. Cele, *Catalysts* **2020**, *10*, 363.
[67] T. Burger, F. Koschany, A. Wenng, O. Thomys, K. Köhler, O. Hinrichsen, *Catal. Sci. Technol.* **2018**, *8*, 5920–5932.
[68] F. I. Saaid, A. Arsyad, N. S. H. Azman, A. Kumar, C.-C. Yang, T.-Y. Tseng, T. Winie, *J. Electroceram.* **2020**, *44*, 183–194.
[69] C. Liu, T. R. Cundari, A. K. Wilson, *J. Phys. Chem. C* **2012**, *116*, 5681–5688.
[70] G. Guan, T. Kida, T. Ma, K. Kimura, E. Abe, A. Yoshida, *Green Chem.* **2003**, *5*, 630–634.
[71] F. Westall, K. Hickman-Lewis, N. Hinman, P. Gautret, K. A. Campbell, J. G. Bréhéret, F. Foucher, A. Hubert, S. Sorieul, A. V. Dass, T. P. Kee, T. Georgelin, A. Brack, *Astrobiology* **2018**, *18*, 259–293.

Manuscript received: December 9, 2022
Accepted manuscript online: March 23, 2023
Version of record online: April 19, 2023